

Realizing spin squeezing with Rydberg interactions in an optical clock

<https://doi.org/10.1038/s41586-023-06360-6>

Received: 14 March 2023

Accepted: 22 June 2023

Published online: 30 August 2023

 Check for updates

William J. Eckner¹, Nelson Darkwah Oppong¹, Alec Cao¹, Aaron W. Young¹, William R. Milner¹, John M. Robinson¹, Jun Ye¹ & Adam M. Kaufman¹✉

Neutral-atom arrays trapped in optical potentials are a powerful platform for studying quantum physics, combining precise single-particle control and detection with a range of tunable entangling interactions^{1–3}. For example, these capabilities have been leveraged for state-of-the-art frequency metrology^{4,5} as well as microscopic studies of entangled many-particle states^{6–11}. Here we combine these applications to realize spin squeezing—a widely studied operation for producing metrologically useful entanglement—in an optical atomic clock based on a programmable array of interacting optical qubits. In this demonstration of Rydberg-mediated squeezing with a neutral-atom optical clock, we generate states that have almost four decibels of metrological gain. In addition, we perform a synchronous frequency comparison between independent squeezed states and observe a fractional-frequency stability of $1.087(1) \times 10^{-15}$ at one-second averaging time, which is 1.94(1) decibels below the standard quantum limit and reaches a fractional precision at the 10^{-17} level during a half-hour measurement. We further leverage the programmable control afforded by optical tweezer arrays to apply local phase shifts to explore spin squeezing in measurements that operate beyond the relative coherence time with the optical local oscillator. The realization of this spin-squeezing protocol in a programmable atom-array clock will enable a wide range of quantum-information-inspired techniques for optimal phase estimation and Heisenberg-limited optical atomic clocks^{12–16}.

The field of metrology has emerged as a compelling frontier for quantum-enhanced technologies¹⁷. For example, the use of entangled states of light has already led to enhanced searches for dark matter¹⁸ and improved detection rates in gravitational-wave sensors¹⁹. Ground-breaking advances in optical-frequency metrology have also positioned atomic clocks as a promising platform for practical applications of entangled states²⁰, as leading optical-clock technologies are now limited by the so-called standard quantum limit (SQL), which is a fundamental bound on the precision of unentangled sensors. Engineering metrologically useful entanglement could therefore lead to more precise time-keeping, as well as improved studies of fundamental symmetries²¹, searches for dark matter²² and measurements of gravity at smaller length scales^{23,24}.

The pursuit of quantum enhancements in optical-frequency measurements introduces a variety of experimental hurdles, as the manipulation of useful entangled states places stringent demands on experimental capabilities. These include high-fidelity atomic-state control, isolation from noise, and either controlled interactions or collective measurements¹⁷. In the face of these challenges, a particularly robust class of entangled states—known as spin-squeezed states (SSSs)—has emerged as a powerful and effective resource for achieving sub-SQL performance in neutral-atom clocks operating in the microwave domain^{1,25–27}. Pioneering experiments have pushed spin squeezing into the optical domain using collective atom-cavity coupling to

generate SSSs on the clock transition in atomic ytterbium^{28,29}. Recently, a cavity-quantum-electrodynamics-based strontium lattice clock showed enhanced angular resolution below the SQL, along with a differential clock measurement between two transportable spin-squeezed ensembles with precision below the quantum-projection-noise limit at the 10^{-17} level³⁰. Such experiments with all-to-all cavity-mediated interactions are a promising route towards scalable spin squeezing. So far, these realizations do not harness microscopic control or detection, or access high-fidelity rotations, which are important ingredients in many proposals for engineering optimal quantum sensors and can aid in reaching performance below the SQL during clock operation^{12–14,14–17}.

Here we experimentally generate and study spin squeezing in a programmable atom-array optical clock to realize measurement performance below the SQL in a differential clock comparison (Supplementary Information). The squeezing protocol we use is based on interactions between atoms that are off-resonantly coupled to a Rydberg state^{31,32}. Using this technique, known as Rydberg dressing^{33–36}, we are able to observe finite-range interactions in arrays of up to 140 atoms. We use the resulting Ising-like Hamiltonian to generate spin squeezing on the optical-clock transition in ⁸⁸Sr (refs. 32,37; Fig. 1a). We characterize this squeezing with the Wineland parameter ξ_W^2 , which serves as an entanglement witness³⁸ and quantifies metrological gain³⁹. Assuming an ideal optical local oscillator, one practical way of understanding the Wineland parameter is that a clock with N atoms and ξ_W^2

¹JILA, University of Colorado and National Institute of Standards and Technology, and Department of Physics, University of Colorado, Boulder, Colorado, USA. ✉e-mail: adam.kaufman@colorado.edu

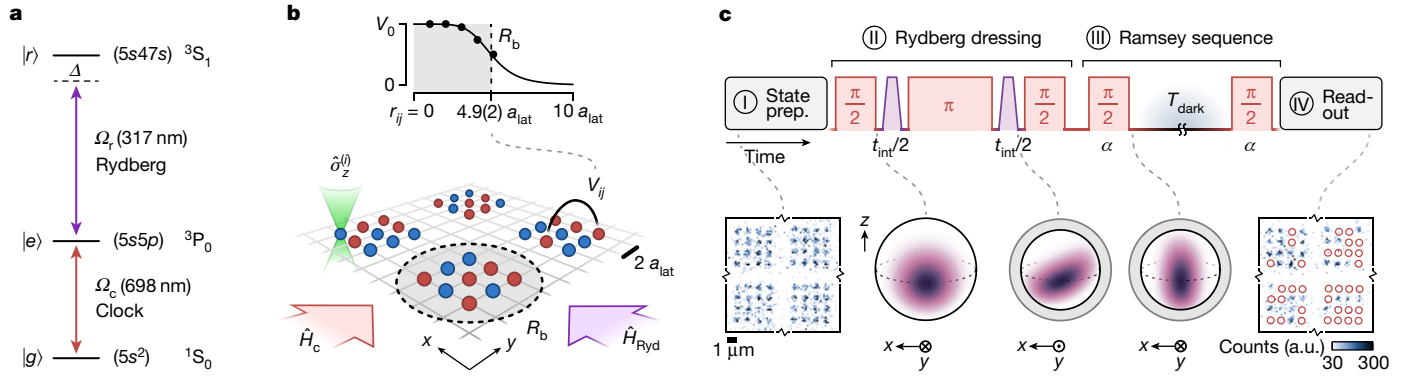


Fig. 1 | Spinsqueezing in a Rydberg-dressed array of ^{88}Sr atoms. a, Atomic states (black lines) and transitions (coloured arrows) of ^{88}Sr relevant for clock interrogation and Rydberg dressing. Rabi frequencies Ω_r and Ω_c indicate the laser coupling between the different states in the experiment and Δ denotes the detuning from $|r\rangle$. **b**, Schematic of the experimental set-up. ^{88}Sr atoms in the states $|g\rangle$ (blue circles) and $|e\rangle$ (red circles) are trapped in an optical lattice (grey lines), with a lattice spacing of $a_{\text{lat}} \approx 575$ nm, and arranged into multiple subarrays. Interactions between atoms at a distance r_{ij} are described by V_{ij} shown in the top plot. Here, black circles are data points (error bars are smaller than the marker size) and the solid black line is a numerical fit (Methods). Laser beams coupling the states in **a** are indicated by coloured arrows and correspond to \hat{H}_c and \hat{H}_{Ryd} (see main text). Optical tweezers (green double cone),

will be able to operate with the same precision as an unentangled, SQL-limited (that is, $\xi_W^2 = 1$) clock with N/ξ_W^2 atoms. Therefore, states with $\xi_W^2 < 1$ ($\xi_W^2 < 0$ dB) contain metrologically useful entanglement. We also perform an exploration of the impact of squeezing on differential clock measurements at times beyond the atom-laser coherence, for which we leverage local single-qubit gates to impart well controlled clock phase shifts for unbiased phase estimation^{40–43} (Supplementary Information).

We create spin squeezing between the $^1\text{S}_0$ ground (denoted $|g\rangle$) and $^3\text{P}_0$ clock (denoted $|e\rangle$) electronic states (Fig. 1a), which are of interest due to their long lifetimes, insensitivity to environmental perturbations and optical carrier frequency. For example, coherent superpositions of these states can persist on the half-minute timescale^{4,23,40}, support long-lived entanglement⁴⁴ and are the foundation for state-of-the-art neutral-atom optical clocks^{23,45}. We generate spin-squeezed ensembles with $\xi_W^2 = -3.8(6)$ dB and $\xi_W^2 = -3.4(3)$ dB in subarrays of $N = 16$ atoms and $N = 70$ atoms, respectively. We then incorporate this spin squeezing into a differential clock comparison between two independent subarrays of atoms. For a measurement time of τ , we observe that the fractional-frequency uncertainty in this comparison averages down with a rate of $1.087(1) \times 10^{-15}/\sqrt{\tau/s}$ for SSSs with $N = 70$ atoms, and reaches an ultimate fractional uncertainty below 3×10^{-17} after a 27.6-min-long measurement. This stability is 2.30(1) dB better than the same measurement performed with coherent spin states (CSSs), and 1.94(1) dB below the SQL in a differential clock comparison.

Our experiments require a combination of global, laser-driven clock rotations—with a typical Rabi frequency of $\Omega_c \approx 2\pi \times 250$ Hz on the $|g\rangle \leftrightarrow |e\rangle$ transition—and Rydberg-mediated interactions. We turn on these interactions by applying a high-power 316.9-nm laser that addresses the $|e\rangle \leftrightarrow |r\rangle = (5s47s)^3\text{S}_1$ transition with a typical Rabi frequency $\Omega_r \approx 2\pi \times 5.5$ MHz and detuning $\Delta \approx 2\pi \times 11$ MHz. When $\Delta \gg \Omega_r$ (‘weak dressing’), this dresses the excited state $|e\rangle$ with an admixture of the Rydberg state $|r\rangle$ and creates a new eigenstate $|e_{\text{dr}}\rangle \approx |e\rangle - \beta|r\rangle$, where $\beta = \Omega_r/(2\Delta)$. Because pairs of Rydberg atoms interact through a van der Waals potential with coefficient C_6 , an effective Hamiltonian for the pseudo-spin states $\{|g\rangle, |e\rangle\}$ can be written as a sum of the two independently controlled terms $\hat{H} = \hat{H}_c + \hat{H}_{\text{Ryd}}$ (refs. 32,36,46)

wavelength 515 nm) enable application of the operator $\hat{\sigma}_z^{(i)}$ to an individual atom i . **c**, Illustration of the experimental sequence for preparing SSSs. In the pulse sequences for II and III, clock and Rydberg laser pulses are shown in red and purple, respectively. Here, α denotes the relative clock laser phase. It is noted that the pulse duration $t_{\text{int}}/2$ is visually enlarged by a factor of about 10^3 . Single-shot images are taken after state preparation (bottom left) and to read out the atomic populations (bottom right). Here, the red circles indicate atoms in $|g\rangle$, which are intentionally removed before the final image. It is noted that the distance between the four subarrays is larger than displayed. Generalized Bloch spheres (bottom centre) illustrate the evolution of the atomic state for a subarray with $N = 4 \times 4 = 16$ atoms (the reduction of the Bloch-sphere radius is not shown to scale).

$$\hat{H}_c = \hbar \Omega_c \hat{S}_x, \quad (1)$$

$$\hat{H}_{\text{Ryd}} = \frac{1}{4} \sum_{i < j} V_{ij} \hat{\sigma}_z^{(i)} \hat{\sigma}_z^{(j)} + \frac{1}{2} \sum_i \delta_i \hat{\sigma}_z^{(i)},$$

where the indices i and j label the atoms in the array, \hbar is the reduced Planck constant, and $\hat{\sigma}_{x,y,z}$ are the Pauli operators. We also denote the collective spin operators $\hat{S}_y = \frac{1}{2} \sum_i \hat{\sigma}_y^{(i)}$ with $y \in \{x, y, z\}$, and associated Bloch vector $\mathbf{S} = (S_x, S_y, S_z)$, where $S_y = \langle \hat{S}_y \rangle$. The parameter δ_i describes a longitudinal field term arising in the effective Hamiltonian³². In the weak-dressing limit, the strength of the interactions is given by a potential $V_{ij} = V_0/[1 + (r_{ij}/R_b)^6]$ where r_{ij} is the distance between atoms i and j , $V_0 = \hbar \beta^2 \Omega_r$, and $R_b = |C_6/(2\Delta)|^{1/6}$. Using pairs of atoms with variable spacing, we can directly measure the shape of the potential^{36,44}. As shown in Fig. 1b, we observe a two-particle interaction that has a spatial dependence consistent with the weak-dressing model, yet with quantitative deviation that is partly attributable to violation of the weak-dressing approximation (Methods).

The spin-squeezing protocol we use largely follows that proposed in ref. 32, illustrated in Fig. 1c, which applies the interaction Hamiltonian \hat{H}_{Ryd} in a spin-echo sequence. This procedure thereby isolates the interaction $\hat{V}_{\text{int}} = \frac{1}{4} \sum_{i < j} V_{ij} \hat{\sigma}_z^{(i)} \hat{\sigma}_z^{(j)}$, which is applied for a total time t_{int} (Methods). We can understand the interaction \hat{V}_{int} by noting that it has a form similar to the one-axis twisting Hamiltonian, but with a finite interaction range set by R_b (ref. 47). We study the squeezing generated with \hat{V}_{int} for small systems by preparing atoms in four square subarrays of $N = 4 \times 4 = 16$ atoms (with an interatomic spacing of $2 a_{\text{lat}}$, where a_{lat} is the lattice spacing). By ensuring that the separation between subarrays is larger than the interaction range R_b , we can treat them as independent populations. This allows us to extract information about their intrinsic quantum noise by performing differential comparisons, which reject most forms of technical noise^{4,44}. The observable for this differential measurement is $\hat{d}_z^{(AB)} = \hat{S}_z / N_A - \hat{S}_z / N_B$, where A and B each label a subarray of atoms, with atom numbers N_A and N_B , respectively (Methods). We can assume that each subarray is a preparation of the same atomic state, and then treat all measurements of $\hat{d}_z^{(AB)}$ as a probe of the same observable, which we call \hat{d}_z . The variance in \hat{d}_z , denoted

Article

σ_α^2 , generally depends on the measurement quadrature, which is set by the angle α , and describes the orientation of the atomic noise distribution. However, in the absence of entanglement or technical noise, σ_α^2 will be independent of α , and governed by quantum-projection noise (QPN), given by

$$\sigma_{\text{QPN}}^2 = \text{Var} \left[\frac{\hat{S}_z^{(A)}}{N_A} - \frac{\hat{S}_z^{(B)}}{N_B} \right]_{\text{CSS}} = \frac{1}{2N}, \quad (2)$$

where we assume $N_A, N_B = N$, as we prepare $N_A \approx N_B$ for all experiments. $\text{Var}[\cdot]_{\text{CSS}}$ denotes the variance of an ideal CSS with $S_z = 0$ for both subarrays A and B.

As shown in Fig. 2a, we can measure σ_α^2 after applying the squeezing protocol to $N = 4 \times 4$ subarrays. We find that the ratio $\sigma_\alpha^2/\sigma_{\text{QPN}}^2$ oscillates sinusoidally with α , and dips below unity near $\alpha \approx 30^\circ$. This measurement demonstrates that SSSs in the system have noise below the QPN limit. However, we must also ensure that this variance reduction is not offset by a reduction in contrast, which could in net reduce the signal-to-noise ratio (Supplementary Information). To verify this, we measure the contrast C of the Ramsey fringe associated with each of these states, and thus the magnitude of the single-ensemble Bloch vector $S = CN/2$.

From the measured quantities σ_α^2 and C , we can determine the Wineland squeezing parameter

$$\xi_W^2 = \frac{N}{2S^2} \text{Var} \left[\hat{S}_z^{(A)} - \hat{S}_z^{(B)} \right]_{\text{min}} = \frac{1}{C^2} \frac{\sigma_{\text{min}}^2}{\sigma_{\text{QPN}}^2}, \quad (3)$$

where σ_{min}^2 denotes the minimum of σ_α^2 , and $\text{Var}[\cdot]_{\text{min}}$ is the minimum variance with respect to α . We determine the optimal α by fitting a cosine to the signal σ_α^2 (Fig. 2a). The parameter ξ_W^2 is then calculated from the variance of an additional, high-statistics dataset taken at the optimal α , as well as the fitted contrast C (see inset of Fig. 2a). Figure 2b shows ξ_W^2 versus interaction time t_{int} for $N = 4 \times 4$ subarrays. By fitting the measured Wineland parameter ξ_W^2 versus t_{int} , we observe a minimum value of $\xi_W^2 = -3.8(6)$ dB, which is comparable to state-of-the-art demonstrations in other optical clocks^{29,30}.

Using site-resolved imaging, we can also probe the microscopic structure of the generated states by analysing the two-particle correlator $g_r^{(2)} = \frac{1}{4} \langle \hat{\sigma}_z^{(i)} \hat{\sigma}_z^{(j)} \rangle - \frac{1}{4} \langle \hat{\sigma}_z^{(i)} \rangle \langle \hat{\sigma}_z^{(j)} \rangle$, where \mathbf{r} is a spatial displacement vector between lattice sites i and j . We measure $g_r^{(2)}$ in larger subarrays to reduce finite-size effects. For $N = 5 \times 14 = 70$ (with spacing $3 a_{\text{lat}}$ along x and $2 a_{\text{lat}}$ along y), we find that the measured $g_r^{(2)}$ agrees qualitatively with theoretical predictions at the optimal interaction time (Methods). In particular, we observe correlations that extend over a range that is similar to the characteristic length scale $R_b \approx 5 a_{\text{lat}}$ of the interaction potential V_{ij} shown in Fig. 1b. For $|\mathbf{r}| < R_b$, we observe correlations that change from negative to positive as a function of α . As expected, the α with minimum Wineland parameter ξ_W^2 exhibits strong negative correlations.

An important question concerns how the Wineland parameter ξ_W^2 changes with increasing atom number N . For the finite-range interactions realized by Rydberg dressing, we expect ξ_W^2 to saturate when the mean interatomic distance becomes much larger than R_b (ref. 32). To probe this regime, we perform additional measurements of the optimal ξ_W^2 with subarrays of $N = 4, N = 9, N = 25$ and $N = 70$ atoms. For each, we employ an empirical fit (Fig. 2b) to determine the optimal Wineland parameter ξ_W^2 , shown in Fig. 2d (Methods). We do not observe a strong dependence on N in the achievable squeezing $1/\xi_W^2$, which saturates to about 4 dB for $N = 9$ and $N = 16$, and is slightly reduced for larger subarrays of $N = 25$ and $N = 70$.

So far, we have focused on the preparation of SSSs. Next, we benchmark their performance in a synchronous optical-frequency comparison between independent atomic ensembles, labelled A and B

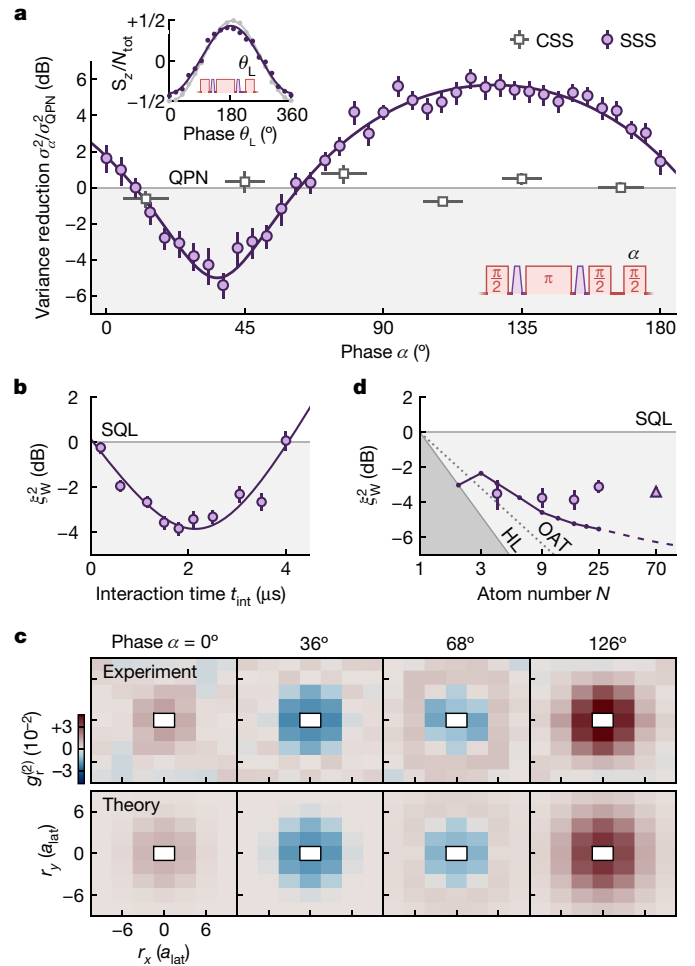


Fig. 2 | Characterization of spin squeezing and finite-range interactions. Unless noted otherwise, the displayed data correspond to $N = 4 \times 4 = 16$ atoms. **a**, Variance reduction $\sigma_\alpha^2/\sigma_{\text{QPN}}^2$ of the CSS (grey squares) and the SSS (purple circles) for variable phase α of the final clock laser pulse and $t_{\text{int}} = 2.4 \mu\text{s}$. Data points for the CSS are binned and the solid purple line is a cosine fit to the data. The top left inset shows S_z/N of the CSS (grey points) and SSS (purple points) for variable phase θ_L , and averaged over subarrays. The solid lines represent fits yielding the contrast $C = 0.97(1)$ for the CSS and $0.83(2)$ for the SSS. **b**, Wineland squeezing parameter ξ_W^2 (purple circles) measured for variable t_{int} . The dark purple line shows an empirical fit to determine the optimal ξ_W^2 . **c**, Two-particle correlator $g_r^{(2)}$ (see main text) in a subarray with $N = 5 \times 14 = 70$ atoms and close to the optimal interaction time, $t_{\text{int}} = 1.6 \mu\text{s}$, for variable phase α and horizontal (vertical) displacement r_x (r_y). The bottom rows show the weak-dressing theory at optimal interaction time for an offset angle $\alpha \rightarrow \alpha - 9.9^\circ$ determined from a fit to the experimental data. We note that the optimal interaction time differs for the experiment and theory shown here (Methods). **d**, Large purple circles correspond to the optimized Wineland squeezing parameter ξ_W^2 measured in square arrays with $N = \sqrt{N} \times \sqrt{N}$ atoms. The triangular marker corresponds to data taken in a rectangular array with $N = 5 \times 14$. The small circles connected by a solid purple line show the theoretical prediction based on weak dressing (dashed purple line indicates subarrays with $N = 5 \times m$ for $N > 25$). The solid and dotted grey lines indicate the Heisenberg limit (HL) and the asymptotic scaling for the one-axis twisting (OAT) Hamiltonian, respectively.

(see insets in Fig. 3). We interrogate both CSSs and SSSs in a Ramsey-interferometry sequence with a variable dark time T_{dark} (see diagram in Fig. 3b). During the dark time, the phases of ensembles A and B precess at their angular clock frequencies ω_A and ω_B , respectively. At the end of the dark time, we then measure the differential phase ϕ between the two ensembles, which is related to the previously defined observable $\hat{d}_z^{(AB)}$ by

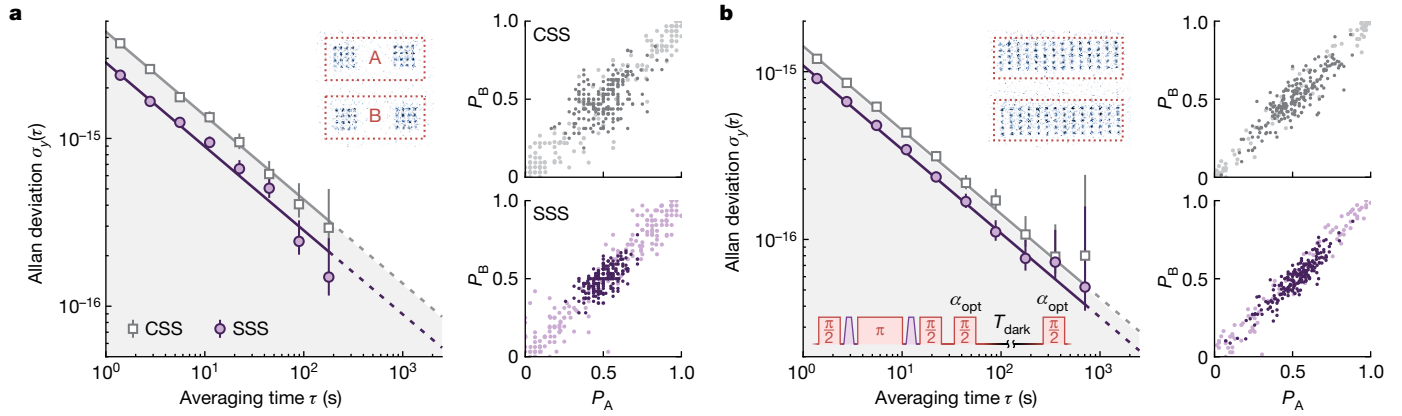


Fig. 3 | Atom-atom stability for CSSs and SSSs. a, b, Overlapping Allan deviation for the differential clock comparison between two subarrays after preparing a CSS (grey squares) or an SSS (purple circles). The subarrays A and B are illustrated in the top right inset of each main panel with $N_{(A,B)} = 2 \times (4 \times 4) = 32$ (a) and $N_{(A,B)} = 5 \times 14 = 70$ (b). The atoms are interrogated with a dark time of $T_{\text{dark}} = 26.0$ ms (a) and 54.5 ms (b) between two $\pi/2$ pulses with the laser phase α_{opt} optimized for the measurement quadrature with lowest noise (see bottom left inset of main panel in b). The solid lines show numerical fits to the data yielding differential stabilities of $2.829(4) \times 10^{-15}/\sqrt{\tau/s}$ and $1.087(1) \times 10^{-15}/\sqrt{\tau/s}$ for the SSS in a and b, respectively. These stabilities are respectively 3.52(1) dB and 1.94(1) dB below the SQL for a differential clock comparison (Supplementary Information), and correspond to a 3.69(2) dB and 2.30(1) dB enhancement over

$$d_z^{(AB)} \approx \frac{C}{2} \phi = \frac{C}{2} (\omega_A - \omega_B) T_{\text{dark}}, \quad (4)$$

when $\phi \ll 1$ (Methods). For ensembles with $N = 32$ (each comprised of two 4×4 subarrays) and $T_{\text{dark}} = 26.0$ ms we observe a fractional-frequency stability of $2.829(4) \times 10^{-15}/\sqrt{\tau/s}$ between two SSSs (Fig. 3a). This corresponds to a 3.52(1) dB enhancement over the SQL in a differential clock comparison (Supplementary Information), and a 3.69(2) dB improvement compared with the same measurement performed with CSSs. With ensembles of size $N = 5 \times 14 = 70$ and $T_{\text{dark}} = 54.5$ ms we realize a stability of $1.087(1) \times 10^{-15}/\sqrt{\tau/s}$ between two SSSs. Assuming the data continue to average as white frequency noise, this implies a final instability below 3×10^{-17} when extrapolated to the full measurement time of 27.6 min. This stability is 1.94(1) dB (2.30(1) dB) below the SQL (CSS) for a differential clock comparison (Supplementary Information). The smaller metrological gain for $N = 70$ could be attributed to a slightly reduced $1/\xi_W^2$ as observed in Fig. 2d. However, the larger-atom-number arrays still allow us to reach a lower absolute measurement uncertainty at fixed averaging time. To the best of our knowledge, these measurements are the first to achieve a fractional-frequency precision below the SQL for a differential clock comparison in a neutral-atom optical clock (Supplementary Information).

One can extend differential frequency comparisons beyond the atom-laser coherence time^{4,23,40,41}. In this regime, the phase of the second $\pi/2$ pulse in a Ramsey interferometer is completely randomized. However, the measured clock-state fractions P_A and P_B of the two ensembles A and B can be plotted parametrically, and trace out an ellipse with an opening angle set by the differential phase ϕ . Given an appropriate atomic noise model, maximum-likelihood estimation (MLE) can be employed to directly measure ϕ . We refer to this as ‘ellipse fitting’⁴³.

We explore the ellipse-fitting approach using two $N = 70$ SSSs. We repeat this measurement for a few different Ramsey dark times and compare the precision to that achieved with comparable CSSs. To extract the measurement uncertainty achieved with CSSs and SSSs, we calculate an Allan deviation σ_ϕ of the measured phase ϕ through a jackknifing procedure⁴¹ (Supplementary Information). The inset in

the CSS. The two right panels in a and b show the excitation probabilities P_A and P_B of subarrays A and B. The light purple and light grey points correspond to a separate measurement, in which the phase of the final $\pi/2$ pulse is varied over 360° to determine the contrast $C = 0.97(1)$ (0.87(1)) in a and $C = 0.96(1)$ (0.86(1)) in b for the CSS (SSS). The Allan deviations in a (b) are calculated from the results of 500 (1,200) measurements, with a cycle time of approximately 1.4 s. In the smaller plots on the right, the dark purple and grey points correspond to results of the first 200 measurements for each dataset. The spread of these data illustrates how much of the Ramsey fringe is sampled when locking the clock laser to the atomic signal (Methods). It is noted how the reduced variance of the SSS compared with the CSS can be seen close to $P_A \approx P_B \approx 0.5$ along the anti-diagonal of this plot.

Fig. 4c shows one such Allan deviation obtained for $T_{\text{dark}} = 1.16$ ms. At this short dark time, the SSS provides an inferred measurement uncertainty that is about 2 dB better than that reached with a CSS. These results suggest that SSSs could improve the precision of ellipse-fitting measurements, yet there remain open theoretical questions regarding the choice of statistical model for the SSSs (Methods). Furthermore, indications of a potential enhancement are gone by $T_{\text{dark}} = 150$ ms. Therefore, this procedure and the associated modelling do not currently allow for higher-precision differential Ramsey measurements than those presented in ref. 4. We leave a detailed study of the technical limitations on squeezing lifetime and how this performance could be extended to longer dark times as a subject for future work. However, we speculate that inhomogeneous light shifts from the optical lattice and the consequent dephasing could play an important role⁴⁴.

In summary, we have employed a Rydberg-dressing protocol to generate up to 3.8(6) dB of spin squeezing on the optical-clock transition in ⁸⁸Sr. This has allowed us to perform a synchronous clock comparison with a stability that is up to 3.52(1) dB below the SQL. The demonstrated protocol establishes an effective approach for reaching entanglement-enhanced optical atomic clocks, and is compatible with other existing experiments^{5,23,40,45}. Looking to the future, a number of questions and avenues of investigation remain. Although the CSS and SSS maintain relative atomic coherence for long Ramsey times out to 5 s, as noted, we observe signs of an inferred enhancement only at short dark times; correcting this disparity could yield improvements, particularly with refined modelling of the underlying distribution of the experimentally produced entangled states. Another important consideration is whether the reported stability enhancements can be combined with state-of-the-art accuracy. To this end, the switchability of the Rydberg interactions allows the entangling operations and Ramsey-based metrology to be fully decoupled, which should reduce systematic effects related to Rydberg excitations. This work sets the stage for fundamental investigations of more sophisticated protocols for generating metrologically useful entangled states for quantum sensing, including protocols that leverage dynamics under more complex spin models^{48,49}, Floquet engineering⁵⁰ or variationally optimized

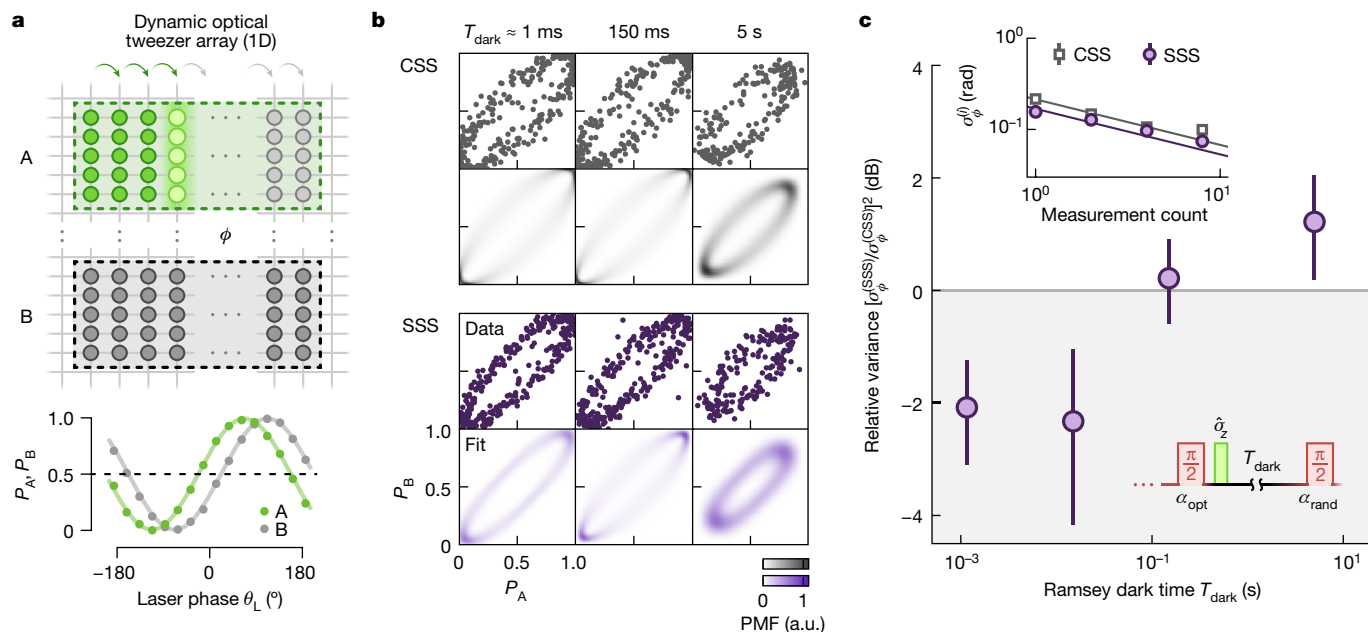


Fig. 4 | Exploring metrology with SSSs in the limit of randomized atom-laser phase. In all panels, we study two subarrays with $N = 5 \times 14 = 70$ each. **a**, Schematic of the phase-shifting procedure. Dynamic optical tweezers (light green circles) collocated with the optical lattice (grey lines) apply local operators $\hat{\sigma}_z^{(i)}$ onto the atoms (green and grey circles). At the bottom, together with a fit (solid lines), an example Ramsey measurement of the phase shift ϕ between subarrays A and B is shown. **b**, Measurements of the probabilities P_A and P_B for variable Ramsey dark time $T_{\text{dark}} = 1.16$ ms, $T_{\text{dark}} = 150$ ms and $T_{\text{dark}} = 5$ s. Here, the relative phase shift takes a value of $\phi \approx 30^\circ$ ($T_{\text{dark}} < 5$ s) or $\phi \approx 40^\circ$ ($T_{\text{dark}} = 5$ s). The first and third

rows show the experimental data for the CSS (grey squares) and the SSS (purple points), respectively. The other rows show the numerically fitted probability mass functions (PMFs; Methods). **c**, Purple circles correspond to the inferred relative variance of the SSS compared with the CSS for variable dark time T_{dark} . Each data point is determined by comparing the Allan deviation σ_ϕ of the estimated-phase uncertainty after averaging over a variable number of measurements. Here, the inset shows an example for $T_{\text{dark}} = 1.16$ ms (error bars smaller than the marker size), and the bottom right schematic illustrates part of the pulse sequence in this measurement.

quantum circuits, even in the regime where the resulting many-body dynamics are challenging to simulate with classical resources^{13,14,51}. Lastly, the single-particle readout and rearrangement demonstrated here could be used to perform mid-circuit measurements in an entangled optical atomic clock to reach Heisenberg-limited performance that is robust to local oscillator noise^{10,15,16,52}.

During the completion of this work, we became aware of related works using Rydberg interactions in a tweezer-array platform⁵³ and long-range interactions in an ion string⁵⁴.

Online content

Any methods, additional references, Nature Portfolio reporting summaries, source data, extended data, supplementary information, acknowledgements, peer review information; details of author contributions and competing interests; and statements of data and code availability are available at <https://doi.org/10.1038/s41586-023-06360-6>.

1. Schleier-Smith, M. H., Leroux, I. D. & Vuletić, V. States of an ensemble of two-level atoms with reduced quantum uncertainty. *Phys. Rev. Lett.* **104**, 073604 (2010).
2. Gross, C. & Bloch, I. Quantum simulations with ultracold atoms in optical lattices. *Science* **357**, 995–1001 (2017).
3. Browaeys, A. & Lahaye, T. Many-body physics with individually controlled Rydberg atoms. *Nat. Phys.* **16**, 132–142 (2020).
4. Young, A. W. et al. Half-minute-scale atomic coherence and high relative stability in a tweezer clock. *Nature* **588**, 408–413 (2020).
5. Madjarov, I. S. et al. An atomic-array optical clock with single-atom readout. *Phys. Rev. X* **9**, 041052 (2019).
6. Fukuhara, T. et al. Spatially resolved detection of a spin-entanglement wave in a Bose-Hubbard chain. *Phys. Rev. Lett.* **115**, 035302 (2015).
7. Islam, R. et al. Measuring entanglement entropy in a quantum many-body system. *Nature* **528**, 77–83 (2015).
8. Kaufman, A. M. et al. Quantum thermalization through entanglement in an isolated many-body system. *Science* **353**, 794–800 (2016).
9. Graham, T. et al. Multi-qubit entanglement and algorithms on a neutral-atom quantum computer. *Nature* **604**, 457–462 (2022).

10. Bluvstein, D. et al. A quantum processor based on coherent transport of entangled atom arrays. *Nature* **604**, 451–456 (2022).
11. Zhang, W.-Y. et al. Functional building blocks for scalable multipartite entanglement in optical lattices. Preprint at <https://arxiv.org/abs/2210.02936> (2022).
12. Tóth, G. & Apellaniz, I. Quantum metrology from a quantum information science perspective. *J. Phys. A* **47**, 424006 (2014).
13. Kaubruegger, R. et al. Variational spin-squeezing algorithms on programmable quantum sensors. *Phys. Rev. Lett.* **123**, 260505 (2019).
14. Kaubruegger, R., Vasilyev, D. V., Schulte, M., Hammerer, K. & Zoller, P. Quantum variational optimization of Ramsey interferometry and atomic clocks. *Phys. Rev. X* **11**, 041045 (2021).
15. Kessler, E. M. et al. Heisenberg-limited atom clocks based on entangled qubits. *Phys. Rev. Lett.* **112**, 190403 (2014).
16. Pezzè, L. & Smerzi, A. Heisenberg-limited noisy atomic clock using a hybrid coherent and squeezed state protocol. *Phys. Rev. Lett.* **125**, 210503 (2020).
17. Pezzè, L., Smerzi, A., Oberthaler, M. K., Schmied, R. & Treutlein, P. Quantum metrology with nonclassical states of atomic ensembles. *Rev. Mod. Phys.* **90**, 035005 (2018).
18. Backes, K. M. et al. A quantum enhanced search for dark matter axions. *Nature* **590**, 238–242 (2021).
19. Tse, M. et al. Quantum-enhanced Advanced LIGO detectors in the era of gravitational-wave astronomy. *Phys. Rev. Lett.* **123**, 231107 (2019).
20. Ludlow, A. D., Boyd, M. M., Ye, J., Peik, E. & Schmidt, P. O. Optical atomic clocks. *Rev. Mod. Phys.* **87**, 637–701 (2015).
21. Sanner, C. et al. Optical clock comparison for Lorentz symmetry testing. *Nature* **567**, 204–208 (2019).
22. Kennedy, C. J. et al. Precision metrology meets cosmology: improved constraints on ultralight dark matter from atom-cavity frequency comparisons. *Phys. Rev. Lett.* **125**, 201302 (2020).
23. Bothwell, T. et al. Resolving the gravitational redshift across a millimetre-scale atomic sample. *Nature* **602**, 420–424 (2022).
24. Zheng, X., Dolde, J., Lim, H. M. & Kolkowitz, S. A lab-based test of the gravitational redshift with a miniature clock network. Preprint at <https://arxiv.org/abs/2207.07145> (2022).
25. Greve, G. P., Luo, C., Wu, B. & Thompson, J. K. Entanglement-enhanced matter-wave interferometry in a high-finesse cavity. *Nature* **610**, 472–477 (2022).
26. Braverman, B. et al. Near-unitary spin squeezing in ¹⁷¹Yb. *Phys. Rev. Lett.* **122**, 223203 (2019).
27. Malia, B. K., Wu, Y., Martínez-Rincón, J. & Kasevich, M. A. Distributed quantum sensing with mode-entangled spin-squeezed atomic states. *Nature* **612**, 661–665 (2022).
28. Pedrozo-Peñafiel, E. et al. Entanglement on an optical atomic-clock transition. *Nature* **588**, 414–418 (2020).
29. Colombo, S. et al. Time-reversal-based quantum metrology with many-body entangled states. *Nat. Phys.* **18**, 925–930 (2022).

30. Robinson, J. M. et al. Direct comparison of two spin squeezed optical clocks below the quantum projection noise limit. Preprint at <https://arxiv.org/abs/2211.08621> (2022).
31. Bouchoule, I. & Mølmer, K. Spin squeezing of atoms by the dipole interaction in virtually excited Rydberg states. *Phys. Rev. A* **65**, 041803 (2002).
32. Gil, L. I. R., Mukherjee, R., Bridge, E. M., Jones, M. P. A. & Pohl, T. Spin squeezing in a Rydberg lattice clock. *Phys. Rev. Lett.* **112**, 103601 (2014).
33. Jau, Y.-Y., Hankin, A., Keating, T., Deutsch, I. H. & Biedermann, G. Entangling atomic spins with a Rydberg-dressed spin-flip blockade. *Nat. Phys.* **12**, 71–74 (2016).
34. Borish, V., Marković, O., Hines, J. A., Rajagopal, S. V. & Schleier-Smith, M. Transverse-field Ising dynamics in a Rydberg-dressed atomic gas. *Phys. Rev. Lett.* **124**, 063601 (2020).
35. Guardado-Sanchez, E. et al. Quench dynamics of a Fermi gas with strong nonlocal interactions. *Phys. Rev. X* **11**, 021036 (2021).
36. Zeiher, J. et al. Coherent many-body spin dynamics in a long-range interacting Ising chain. *Phys. Rev. X* **7**, 041063 (2017).
37. Van Damme, J., Zheng, X., Saffman, M., Vavilov, M. G. & Kolkowitz, S. Impacts of random filling on spin squeezing via Rydberg dressing in optical clocks. *Phys. Rev. A* **103**, 023106 (2021).
38. Friis, N., Vitagliano, G., Malik, M. & Huber, M. Entanglement certification from theory to experiment. *Nat. Rev. Phys.* **1**, 72–87 (2019).
39. Wineland, D. J., Bollinger, J. J., Itano, W. M., Moore, F. L. & Heinzen, D. J. Spin squeezing and reduced quantum noise in spectroscopy. *Phys. Rev. A* **46**, R6797–R6800 (1992).
40. Zheng, X. et al. Differential clock comparisons with a multiplexed optical lattice clock. *Nature* **602**, 425–430 (2022).
41. Marti, G. E. et al. Imaging optical frequencies with 100 μ Hz precision and 1.1 μ m resolution. *Phys. Rev. Lett.* **120**, 103201 (2018).
42. Young, A. W., Eckner, W. J., Schine, N., Childs, A. M. & Kaufman, A. M. Tweezer-programmable 2D quantum walks in a Hubbard-regime lattice. *Science* **377**, 885–889 (2022).
43. Stockton, J. K., Wu, X. & Kasevich, M. A. Bayesian estimation of differential interferometer phase. *Phys. Rev. A* **76**, 033613 (2007).
44. Schine, N., Young, A. W., Eckner, W. J., Martin, M. J. & Kaufman, A. M. Long-lived Bell states in an array of optical clock qubits. *Nat. Phys.* **18**, 1067–1073 (2022).
45. McGrew, W. F. et al. Atomic clock performance enabling geodesy below the centimetre level. *Nature* **564**, 87–90 (2018).
46. Henkel, N., Nath, R. & Pohl, T. Three-dimensional roton excitations and supersolid formation in Rydberg-excited Bose–Einstein condensates. *Phys. Rev. Lett.* **104**, 195302 (2010).
47. Kitagawa, M. & Ueda, M. Squeezed spin states. *Phys. Rev. A* **47**, 5138–5143 (1993).
48. Young, J. T., Muleady, S. R., Perlin, M. A., Kaufman, A. M. & Rey, A. M. Enhancing spin squeezing using soft-core interactions. *Phys. Rev. Res.* **5**, L012033 (2023).
49. Block, M. et al. A universal theory of spin squeezing. Preprint at <https://arxiv.org/abs/2301.09636> (2023).
50. Geier, S. et al. Floquet Hamiltonian engineering of an isolated many-body spin system. *Science* **374**, 1149–1152 (2021).
51. Marciniak, C. D. et al. Optimal metrology with programmable quantum sensors. *Nature* **603**, 604–609 (2022).
52. Bowden, W., Vianello, A., Hill, I. R., Schioppa, M. & Hobson, R. Improving the Q factor of an optical atomic clock using quantum nondemolition measurement. *Phys. Rev. X* **10**, 041052 (2020).
53. Bornet, G. et al. Scalable spin squeezing in a dipolar Rydberg atom array. Preprint at <https://arxiv.org/abs/2303.08053> (2023).
54. Franke, J. et al. Quantum-enhanced sensing on an optical transition via emergent collective quantum correlations. Preprint at <https://arxiv.org/abs/2303.10688> (2023).

Publisher's note Springer Nature remains neutral with regard to jurisdictional claims in published maps and institutional affiliations.

© This is a U.S. Government work and not under copyright protection in the US; foreign copyright protection may apply 2023

Hybrid optical-clock platform

The core elements of the programmable clock platform are shown in Fig. 1b, and are based on a recently demonstrated hybrid tweezer-lattice architecture^{42,44}. We can trap atoms in both a dynamically configurable optical tweezer array and a collocated two-dimensional (2D) optical lattice, each of which exhibits distinct and enabling features for the work presented here. In particular, the optical tweezer array allows for rapid initial loading, deterministic rearrangement into nearly arbitrary patterns within the 2D lattice and the application of controlled, local light shifts, shown schematically in Fig. 1b. The 2D lattice, in contrast, offers several thousand sites in which we can perform ground-state cooling, single-site-resolved imaging and high-fidelity global rotations on the clock transition.

Array initialization

In this work, atom arrays in the optical lattice are initialized via a combination of stochastic loading, detection, deterministic rearrangement with optical tweezers and high-fidelity optical cooling. First, an array of 515-nm tweezers is stochastically loaded from a cold atomic cloud. Light-assisted collisions result in an occupation of zero or one atoms in each tweezer with approximately equal probability⁵⁵. These atoms are implanted into a single 2D layer of a three-dimensional (3D) optical lattice operated close to the clock-magic wavelength of 813.4 nm, and imaged with a combined loss and infidelity of <0.5% (refs. 42,44). The loading procedure, beginning from a hot thermal gas and ending with atoms near the motional ground state of single lattice sites, takes approximately 300 ms, and each image takes about 150 ms. On the basis of these images, and using the optical tweezers, the atoms are rearranged into nearly arbitrary patterns in the lattice^{56–58}. The per-atom success probability for filling a given target pattern can be as high as 99.5%; however, 98% is typical for the data appearing throughout this work. As a representative case, we note that, for the data in Fig. 3, the addition of rearrangement lengthens the sequence by roughly 200 ms. However, this could be improved in future work⁵⁹. After rearrangement, an additional image confirms that the target pattern has been prepared successfully. It is noted that we do not always enforce that the atom array is free of defects, as summarized in the ‘Post-selection’ section. Finally, the rearranged atoms are cooled to their 3D motional ground state via resolved sideband cooling on the $^1S_0 \leftrightarrow ^3P_1$ transition^{42,44}.

In all measurements presented in Figs. 1–4, we prepare the atomic array with a square or rectangular pattern that corresponds to 2 or 4 individual subarrays of size $N = 4$ atoms up to $N = 70$ atoms. By spacing the subarrays sufficiently far apart ($\geq 12 a_{\text{lat}}$), we can treat them as independent atomic ensembles. The spacing between atoms in a subarray is generally chosen to be $2 a_{\text{lat}}$. For $N = 4$ and $N = 70$, the spacing is increased to $(3, 2) a_{\text{lat}}$ along the (x, y) directions. We note that this choice is motivated by a slightly improved fidelity of the array initialization, but does not significantly affect the attainable squeezing performance.

Post-selection

For the data in Figs. 1 and 2, we post-select on the fraction of target sites in a subarray that are successfully loaded with an atom (‘Array initialization’), which we refer to as the fill fraction. The post-selection criterion for all datasets is an initial fill fraction of $\geq 92\%$. As we initialize multiple subarrays on each run of the experiment, we note that subarrays are post-selected on an individual level; that is, for a given experimental trial, we only exclude pairs of subarrays with at least one subarray that has a fill fraction below the 92% threshold.

We do not post-select on fill fraction for the stability and ellipse-fitting datasets shown in Figs. 3 and 4. However, for the CSS shown in Fig. 3b, there was a single experimental trial in which all subarrays had a fill fraction of zero (that is, no atoms were initialized in the target pattern),

and we exclude this trial from our analysis. Similarly, in Fig. 4b,c—and in ascending order with Ramsey dark time—the SSS (CSS) data have (zero, one, two, one) ((zero, two, two, one)) experimental trials in which all subarrays had fill fractions of zero; these trials are removed from the corresponding datasets. As we calculate the Allan deviation versus number of binned data points M (as opposed to averaging time τ), neglecting these points in the analysis does not affect the inferred stabilities.

Clock rotations and state detection

After initializing the atom array, a magnetic field of about 275 G is turned on to allow the $|g\rangle \leftrightarrow |e\rangle$ transition to be resonantly driven with a typical Rabi frequency of $\Omega_c \approx 2\pi \times 250$ Hz (refs. 44,60). We note that for the data shown in Fig. 1b and the $N = 2 \times 2 = 4$ data in Fig. 2d, we employ a smaller magnetic field of about 55 G. The ultra-narrow clock laser is stabilized to a cryogenic silicon cavity, as described in refs. 61,62. Arbitrary clock rotations can be performed by controlling the duration and phase of pulses from this drive laser using an acousto-optic modulator. We typically measure a π -pulse fidelity of $\geq 99\%$. After preparing a SSS or CSS and interrogating the atoms, we detect their electronic state. To this end, we apply 461-nm blowaway light, resonant with the dipole-allowed $|g\rangle \leftrightarrow ^1P_1$ transition, which heats $|g\rangle$ atoms out of the trap. This procedure projects each atom into either the $|g\rangle$ state (detected as loss) or $|e\rangle$ state (detected as survival). For further details on state detection and imaging, see ref. 44.

To sample the squeezed quadrature of a SSS, we need to align it with projective measurements of the \hat{S}_z -basis states $|g\rangle$ and $|e\rangle$. To achieve this, we change the phase of the drive Ω_c by a variable angle α after the Rydberg-dressing pulse sequence (II in Fig. 1c). At this stage the Bloch vector is aligned parallel to the z axis, that is, $\mathbf{S} = \pm 5(0, 0, 1)$, and a phase change of the drive can be understood as a global \hat{S}_z rotation by α , which does not change the magnitude or direction of the Bloch vector. After applying another $\pi/2$ pulse, the atomic noise distribution is rotated by α with respect to the equatorial plane of the generalized Bloch sphere (as illustrated in Fig. 1c). To maximize the metrological gain in stability and ellipse-fitting measurements, we experimentally determine the optimal α before each measurement and choose the clock laser phase for the final two $\pi/2$ pulses in the Ramsey sequence appropriately (III in Fig. 1c).

Local $\hat{\sigma}_z$ operations

We use 515-nm optical tweezers to introduce locally controlled light shifts across the array. These operations can also be understood as local $\hat{\sigma}_z$ rotations. It is noted that in combination with arbitrary global single-qubit rotations, this technique provides access to a universal set of single-qubit gates. For the data presented in Fig. 4, and as described in the main text, we demonstrate this control by creating a homogeneous light shift across a 70-atom subarray. To realize this operation, a single column of tweezers is turned on and the desired light shift is applied to one column of atoms. This is iterated column-by-column across the 2D array (Fig. 4a). The primary motivation for only applying one-dimensional columns of tweezers at any given time is to ensure that we have a sufficient number of degrees of freedom to independently and arbitrarily tune the phase shift at each site. For a further discussion of the performance of this protocol, see Supplementary Information.

Rydberg drive and parameters

Our ultraviolet laser system for addressing the $|e\rangle \leftrightarrow |r\rangle$ transition is detailed in ref. 44. We switch on (off) this laser by simultaneously ramping Ω_c to its maximum (minimum) value and Δ to its minimum (maximum). Typically, Ω_c ramps from 0 to about 5.5 MHz, and Δ ramps from about $2\pi \times 33$ MHz to about $2\pi \times 11$ MHz. These ramps have a duration of 225 ns, and are implemented by linearly sweeping the radio-frequency power and frequency to an acousto-optic modulator, following the

procedure in ref. 44. We note that the interaction times t_{int} quoted in this work do not include the duration of the ramps.

For each measurement in this work, we characterize the relevant parameters of the Rydberg drive $\hat{H}_{\text{Ryd}}: \Omega_r$ and Δ . As the Rydberg laser is locked to a high-finesse cavity, we control Δ directly by changing the radio frequency of a cavity offset lock. The Rabi frequency Ω_r is determined by driving on-resonance ($\Delta = 0$) Rabi oscillations for isolated single atoms.

For theoretical calculations ('Weak-dressing theory'), we assume $C_6 \approx 2\pi \times 9.1 \text{ GHz } \mu\text{m}^6$. We estimate this value from experimental measurements of the two-photon $|ee\rangle \rightarrow |rr\rangle$ transition frequency for interatomic distances r_{ij} between $3 a_{\text{lat}}$ and $7 a_{\text{lat}}$. However, this measurement is susceptible to a variety of systematic effects, such as stray electric fields, which we do not characterize. Therefore, this value for C_6 may not be representative of Rydberg interactions in conditions that differ from those used in this work.

Interaction potential

Figure 1b shows a measurement of the soft-core potential V_{ij} that describes the two-particle interactions in the system. For this measurement, we initialize the atom array with a few isolated pairs of atoms at variable distance $r_{0i} = (1, 2, 3, 4, 5) a_{\text{lat}}$. We then apply the Rydberg-dressing pulse sequence (II in Fig. 1c) followed by an additional $\pi/2$ clock pulse. A subsequent measurement of the atomic population corresponds to a measurement of the S_z observable that oscillates with the frequency ω . We extract ω from a damped cosine fit and relate it to $V(r_{0i})$ by diagonalizing the two-particle Hamiltonian ($i, j = 0, 1$; equation (1)). Finally, a numerical fit to $\omega [1 + (r_{0i}/\tilde{R}_b)^6]^{-1}$ yields the relevant fitted parameters $\tilde{V}_0 = 2\hbar\omega = h \times 46.4(4) \text{ kHz}$ and $\tilde{R}_b = 4.9(2) a_{\text{lat}}$. Notably, the interaction strength V_0 deviates significantly from the one obtained from the relations $V_0 = \beta^3 \Omega_r \approx h \times 80.6 \text{ kHz}$ and the independently determined parameters Ω_r and Δ . This could be attributed to the relatively large $\beta = \Omega_r/(2\Delta) \approx 0.25$ employed throughout this work. In particular, we find that the results from an exact-diagonalization calculation (Supplementary Information) are much closer to \tilde{V}_0 .

Wineland parameter

Each value of the Wineland parameter ξ_W^2 shown in Fig. 2b,d involves measuring the contrast C as well as the variance reduction $\sigma_a^2/\sigma_{\text{QPN}}^2$. Example measurements for these quantities are shown in Fig. 2a for the case of $N = 4 \times 4 = 16$. It is noted that the quantity σ_{QPN} is calculated for the actual atom number obtained under the post-selection criterion explained in 'Post-selection'. To reduce the statistical uncertainty of ξ_W^2 , we first obtain the optimal α by a measurement and a numerical cosine fit like the one shown in Fig. 2a. Subsequently, the value of the minimum variance reduction $\sigma_a^2/\sigma_{\text{QPN}}^2$ is determined from an additional high-statistics measurement at the optimal α . We employ this procedure for all atom numbers except for $N = 2 \times 2 = 4$, where the minimum variance reduction is obtained directly from a cosine fit. For all atom numbers, we measure the Wineland parameter ξ_W^2 for a range of different interaction times t_{int} . To obtain the optimal ξ_W^2 (and t_{int}), we employ an empirical fit described by $ae^{-\Gamma_a t_{\text{int}}} + be^{-\Gamma_b t_{\text{int}}}$ with fit parameters a, b and Γ_a, Γ_b . An example plot of this functional form together with experimental data can be found in Fig. 2b (dark purple line). The values of ξ_W^2 plotted in Fig. 2d and quoted in the main text are obtained from the fit parameters and the resulting minimum of the above function.

Atom-atom stability

For the differential frequency comparisons shown in Fig. 3, we employ Ramsey spectroscopy. At the end of the dark time T_{dark} , we measure the signal

$$d_z^{(\text{AB})} = \frac{C}{2} [\sin(\omega_A T_{\text{dark}}) - \sin(\omega_B T_{\text{dark}})] \quad (5)$$

where $\omega_A T_{\text{dark}}$ ($\omega_B T_{\text{dark}}$) is the phase accrued by ensemble A (B) during the dark time. As $(\omega_A - \omega_B) T_{\text{dark}}$ is generally small, $(\omega_A - \omega_B) \approx 2d_z^{(\text{AB})}/(CT_{\text{dark}})$. We measure this angular frequency difference multiple times with a regular time interval of about 1.4 s between individual data points. This allows us to obtain the differential stability between A and B by calculating the overlapping Allan deviation for a variable total averaging time τ (Fig. 3). It is noted that we employ a low-gain digital servo to lock the laser onto the atomic resonance position during atom-atom stability measurements. This servo ensures that the atomic populations remain near the optimal value by controlling the frequency of the clock laser beam using an acousto-optical modulator.

Error bars and model fitting

Throughout this work, fitted parameters corresponding to the CSS are extracted via MLE under the assumption that the underlying distribution is binomial, whereas the corresponding parameters for the SSS are extracted via least-squares fits weighted by $1/N_i$, where N_i is the number of atoms loaded on a given shot i of the experiment. For the contrasts contributing to Figs. 2 and 3, confidence intervals are determined by non-parametric bootstrap using the basic method⁶³. Errors in other fitted parameters are determined from jackknifing, that is, the displayed error bars correspond to the jackknife estimate for the standard error⁶⁴. Unless noted otherwise, numerical least-squares fits weight the data points with their inverse variance. For the data corresponding to the variance reduction in Fig. 2a, error bars of the variance are also determined by jackknifing.

Weak-dressing theory

For the weak-dressing theory shown in Fig. 2d, we directly employ the analytical results given in ref. 32 to obtain the relevant experimental parameters $C, \sigma_a^2/\sigma_{\text{QPN}}^2$ and ξ_W^2 . We note that the ramps of the Rabi frequency and detunings ('Rydberg drive and parameters') are neglected in these calculations. The atom numbers for the weak-dressing theory curve shown in Fig. 2d (light purple line) are $N = 1 \times 2, 1 \times 3, 2 \times 2, \dots, 5 \times 5$ and $5 \times m$ with $m = 6, 7, \dots, 20$. Here, the spacing between atoms is set to $2 a_{\text{lat}}$. Although the independently determined experimental parameters Ω_r and Δ in each of the measurements aggregated in Fig. 2d slightly differ, the weak-dressing theory is calculated for the parameters of the $N = 4 \times 4 = 16$ dataset.

Following ref. 65, we find the following expression for the relevant two-particle correlator shown in Fig. 2c (spatial correlations)

$$g_{ij}^{(2)} = \frac{1}{4} (P_{ij}^- - P_{ij}^+) \sin^2 \alpha + \frac{1}{4} \sin \alpha \cos \alpha \sin \varphi_{ij} \times \left(\prod_{k \neq i,j} \cos \varphi_{ik} + \prod_{k \neq i,j} \cos \varphi_{jk} \right) \quad (6)$$

with the expression $P_{ij}^\pm = \frac{1}{2} \prod_{k \neq i,j} \cos(\varphi_{ki} \pm \varphi_{kj})$ and the interaction phase $\varphi_{ij} = V_{ij} t_{\text{int}} / (2\hbar)$. The above quantity is then related to $g_{\mathbf{r}}^{(2)}$ mentioned in the main text using the distances r_{ij} between atoms in the experimentally prepared subarray with atom number $N = 5 \times 14 = 70$. Here the spacing between atoms is set to $(3, 2) a_{\text{lat}}$ along the x and y axes to match the experimental realization. The theory shown in Fig. 2c is calculated at the optimal interaction time by first minimizing ξ_W^2 calculated with the weak-dressing theory from ref. 32. In the limit $N \rightarrow \infty$ and for a spacing of $(2, 2) a_{\text{lat}}$, the results from ref. 32 predict that the Wineland squeezing parameter should saturate to a value of $\xi_\infty^2 \approx -8 \text{ dB}$.

Ellipse fitting

One consideration in ellipse fitting is that measurements of $\phi \approx 0$ have biased results⁴¹ (Supplementary Information). To operate away from this point, we use the local control afforded by optical tweezer arrays to apply a homogeneous phase offset of $\phi \approx 30^\circ$ to one of the two ensembles (Fig. 4a). To address residual drift in this phase-shifting protocol

Article

(‘Local $\hat{\sigma}_z$ operations’), we interleave measurements with the CSS and SSS so that they probe the same ϕ . Owing to the interleaved operation of ellipse measurements, we choose to parameterize the Allan deviation in terms of number of measurements (as opposed to averaging time τ). In addition, we intentionally randomize the laser phase of the final $\pi/2$ pulse in the interferometer, which ensures uniform sampling of the ellipse traced out by P_A and P_B , independent of the atom-laser coherence time. Figure 4b shows how the data cluster near an ellipse with an opening angle of about 30° . The rows below the data in Fig. 4b depict the fitted noise distributions (Supplementary Information), which show good agreement with the experimental data.

For the MLE in Fig. 4, we must model noise about the mean excitation fractions of the two ensembles. As mentioned in the main text, one challenge associated with ellipse fitting is that we lack a detailed understanding of the noise distribution for the SSS. In this section, we introduce an empirical model for SSSs, which we use to perform MLE. However, we note that future theoretical work will be required to assess the accuracy of this model.

The empirical model we use to fit data in the main text is defined by

$$f(p_A, p_B, \phi, C, y_0, \zeta) = \frac{1}{2\pi} \int_0^{2\pi} f_\theta(p_A, p_B, \phi, C, y_0, \zeta) d\theta. \quad (7)$$

Here, $p_{A,B}$ are specific measurement values for the observables $\hat{P}_{A,B} = 1/2 + \hat{S}_z^{(A,B)}/N_{A,B}$, which correspond to the mean excitation fraction in each ensemble. In addition, f_θ is the probability mass function for the two ensembles with a specified atom-laser phase θ , and takes the form

$$f_\theta(p_A, p_B | \phi, C, y_0, \zeta) = \frac{1}{\mathcal{N}_A \mathcal{N}_B} \left[\binom{N}{k_A} P_A^{k_A} (1 - P_A)^{N - k_A} \right]^{1/\zeta^2(\theta)} \times \left[\binom{N}{k_B} P_B^{k_B} (1 - P_B)^{N - k_B} \right]^{1/\zeta^2(\theta + \phi)}. \quad (8)$$

In this equation, we take $N_A, N_B = N$, $k_{A,B} = p_{A,B}N$ and $P_{A,B} = \langle \hat{P}_{A,B} \rangle$ with

$$P_A = \frac{C}{2} \cos(\theta) + y_0 \quad (9)$$

$$P_B = \frac{C}{2} \cos(\theta + \phi) + y_0.$$

We refer to θ as the atom-laser phase and ϕ as the differential phase; y_0 is an offset. We take C and y_0 to be the same for both ensembles. Finally, $\mathcal{N}_{A,B}$ are normalization factors, and

$$\zeta^2(\theta) = \zeta_0^2 \sin^2(\theta) + \zeta_1^2 \cos^2(\theta). \quad (10)$$

We note that when $\zeta = (1, 1)$, f_θ is simply the product of binomial distributions and representative of a CSS. By design, ζ_0 then plays an analogous role to the squeezing parameter in the large- N limit, where—by the central limit theorem for the binomial distribution— f_θ converges to the product of normal distributions (as long as $P_A, P_B \in (0, 1)$). However, we emphasize that the model parameters $\zeta = (\zeta_0, \zeta_1)$ do not directly correspond to the squeezing or anti-squeezing present in the state. Nevertheless, we define the likelihood function

$$\mathcal{L}(\phi, C, y_0, \zeta | A) = \prod_{i \in I} f(p_A^{(i)}, p_B^{(i)} | \phi, C, y_0, \zeta) \quad (11)$$

where $p_A^{(i)}, p_B^{(i)}$ are the measurement results for a given trial index i in the full set of measurement indices I , and $A = \{(p_A^{(i)}, p_B^{(i)}) | i \in I\}$ is the corresponding set of measurements.

To extract the precision with which we are able to infer the parameter ϕ , we split our data into a calibration dataset $A_{\text{cal}} = \{(p_A^{(i)}, p_B^{(i)}) | i \in I_{\text{cal}}\}$,

and a measurement dataset $A_m = \{(p_A^{(i)}, p_B^{(i)}) | i \in I_m\}$. Here, the set I_{cal} contains a random selection of half of the indices i from 0 to $n - 1$, where n is the total number of measurements, and I_m contains the remaining indices. For consistency, we use the same random samplings for both the SSS and CSS. The role of the calibration dataset is to extract estimates of the parameters C, y_0 and ζ , as well as the uncertainty in these estimates. We characterize these uncertainties using non-parametric bootstrap, and resample the data in A_{cal} a total of 50 times. For a given bootstrap sample A_B , maximizing the likelihood $\mathcal{L}(\phi, C, y_0, \zeta | A_B)$ yields a set of inferred parameters $(\phi_{\text{cal}}, C_{\text{cal}}, y_{\text{cal}}, \zeta_{\text{cal}})$. We discard ϕ_{cal} , and construct a new likelihood function for each $(C_{\text{cal}}, y_{\text{cal}}, \zeta_{\text{cal}})$:

$$\mathcal{L}^B(\phi | A) = \mathcal{L}(\phi, C_{\text{cal}}, y_{\text{cal}}, \zeta_{\text{cal}} | A). \quad (12)$$

We use the corresponding likelihood function calibrated by the original (not resampled) dataset A_{cal} to extract the value of ϕ , along with its statistical variance and Allan deviation, from the measurement data A_m . Repeating this procedure using each $\mathcal{L}^B(\phi | A_m)$ allows us to estimate the effect of calibration errors in the secondary parameters C, y_0 and ζ , independent of statistical uncertainty in the measurement data. The error bars appearing in Fig. 4c correspond to the quadrature sum of these calibration errors with the statistical uncertainty.

To compute the overlapping Allan deviation for each bootstrap sample of calibration parameters, we follow the recipe for jackknifing described in ref. 41 and calculate the amount that each measurement i pulls the overall phase estimate:

$$\phi_i^{\text{JK}} = \frac{n}{2} \phi' - \left(\frac{n}{2} - 1 \right) \phi'_{\neq i} \quad (13)$$

where $n/2$ is the number of points in the measurement set A_m , and ϕ' and $\phi'_{\neq i}$ are defined as:

$$\phi'_{\neq i} = \operatorname{argmax}_{\phi \in [0, \pi]} [\mathcal{L}^B(\phi | A_m \setminus i)]$$

$$\phi' = \operatorname{argmax}_{\phi \in [0, \pi]} [\mathcal{L}^B(\phi | A_m)]. \quad (14)$$

Here, $A_m \setminus i$ refers to the dataset A_m with element $(p_A^{(i)}, p_B^{(i)})$ removed.

The stabilities in Fig. 4c are calculated by taking the overlapping Allan deviation of the single-shot estimates of the differential phase, ϕ_i^{JK} . We plot the Allan deviation as a function of the number of measurements m (Fig. 4c), which is related to the total measurement time τ by $\tau = mT_{\text{cycle}}$, where T_{cycle} is the cycle time of the experiment. For a direct comparison between the SSS and CSS, we use the same procedure and model to compute the Allan deviation in each case, and plot the ratio in Fig. 4c. As the distribution f converges to the model for a CSS in the limit where $\zeta_0 = \zeta_1 = 1$, this procedure should not underfit CSS data.

Data availability

The experimental data presented in this article are available from the corresponding author upon reasonable request. Source data are provided with this paper.

Code availability

The code used for analysis and simulation in this work is available from the corresponding author upon reasonable request.

55. Norcia, M. A., Young, A. W. & Kaufman, A. M. Microscopic control and detection of ultracold strontium in optical-tweezer arrays. *Phys. Rev. X* **8**, 041054 (2018).
56. Kumar, A., Wu, T.-Y., Giraldo, F. & Weiss, D. S. Sorting ultracold atoms in a three-dimensional optical lattice in a realization of Maxwell’s demon. *Nature* **561**, 83–87 (2018).
57. Endres, M. et al. Atom-by-atom assembly of defect-free one-dimensional cold atom arrays. *Science* **354**, 1024–1027 (2016).

58. Barredo, D., De Léséleuc, S., Lienhard, V., Lahaye, T. & Browaeys, A. An atom-by-atom assembler of defect-free arbitrary two-dimensional atomic arrays. *Science* **354**, 1021–1023 (2016).
59. Young, A. W. et al. An atomic boson sampler. Preprint at <https://arxiv.org/abs/2307.06936> (2023).
60. Taichenachev, A. V. et al. Magnetic field-induced spectroscopy of forbidden optical transitions with application to lattice-based optical atomic clocks. *Phys. Rev. Lett.* **96**, 083001 (2006).
61. Matei, D. G. et al. 1.5 μm lasers with sub-10 mHz linewidth. *Phys. Rev. Lett.* **118**, 263202 (2017).
62. Oelker, E. et al. Demonstration of 4.8×10^{-17} stability at 1 s for two independent optical clocks. *Nat. Photon.* **13**, 714–719 (2019).
63. Carpenter, J. & Bithell, J. Bootstrap confidence intervals: when, which, what? A practical guide for medical statisticians. *Stat. Med.* **19**, 1141–1164 (2000).
64. Efron, B. & Stein, C. The jackknife estimate of variance. *Ann. Stat.* **9**, 586–596 (1981).
65. van den Worm, M., Sawyer, B. C., Bollinger, J. J. & Kastner, M. Relaxation timescales and decay of correlations in a long-range interacting quantum simulator. *New J. Phys.* **15**, 083007 (2013).

Acknowledgements We acknowledge earlier contributions to the experiment from M. A. Norcia and N. Schine and discussions with S. Geller, R. B. Hutson, W. F. McGrew, S. R. Muleady, A. M. Rey, N. Schine, M. Schleier-Smith, J. K. Thompson, J. T. Young and P. Zoller. We thank S. Geller, S. R. Muleady, J. K. Thompson and P. Zoller for reading the paper and comments; and A. Aepli, D. Kedar, K. Kim, B. Lewis, M. Miklos, Y. M. Tso, W. Warfield, L. Yan and Z. Yao

for discussions and contributions to the clock laser system. This material is based on work supported by the Army Research Office (W911NF-19-1-0149 and W911NF-19-1-0223), Air Force Office for Scientific Research (FA9550-19-1-0275), National Science Foundation QLCI (OMA-2016244), US Department of Energy, Office of Science, National Quantum Information Science Research Centers, Quantum Systems Accelerator, and the National Institute of Standards and Technology. We also acknowledge funding from Lockheed Martin. W.J.E. acknowledges support from the NDSEG Fellowship; N.D.O. acknowledges support from the Alexander von Humboldt Foundation; and A.C. acknowledges support from the NSF Graduate Research Fellowship Program (grant number DGE2040434).

Author contributions W.J.E., N.D.O., A.C., A.W.Y. and A.M.K. built and operated the optical lattice and tweezer apparatus. The silicon-crystal stabilized clock laser was operated by W.R.M., J.M.R. and J.Y. All authors contributed to data analysis and development of the paper.

Competing interests The authors declare no competing interests.

Additional information

Supplementary information The online version contains supplementary material available at <https://doi.org/10.1038/s41586-023-06360-6>.

Correspondence and requests for materials should be addressed to Adam M. Kaufman.

Peer review information *Nature* thanks Sebastian C. Carrasco, Michael Goertz and the other, anonymous, reviewer(s) for their contribution to the peer review of this work. Peer reviewer reports are available.

Reprints and permissions information is available at <http://www.nature.com/reprints>.